Sharp-edge-based acoustofluidic chip capable of programmable pumping, mixing, cell focusing and trapping

Author(s):
Pavlic, Alen; Harshbarger, Cooper; Rosenthaler, Luca; Snedeker, Jess Gerrit; Dual, Jürg

Publication date:
2023-02

Permanent link:
https://doi.org/10.3929/ethz-b-000595988

Originally published in:
Physics of Fluids 35(2), https://doi.org/10.1063/5.0133992

Physics of Fluids ARTICLE scitation.org/journal/phf

Sharp-edge-based acoustofluidic chip capable of programmable pumping, mixing, cell focusing, and trapping

Cite as: Phys. Fluids **35**, 022006 (2023); doi: 10.1063/5.0133992
Submitted: 7 November 2022 · Accepted: 25 January 2023 ·
Published Online: 13 February 2023

Alen Pavlic,[1,a)] Cooper Lars Harshbarger,[1,2,3] Luca Rosenthaler,[1] Jess Gerrit Snedeker,[2,3] and Jürg Dual[1]

AFFILIATIONS

[1]Institute for Mechanical Systems, Swiss Federal Institute of Technology Zurich, Zurich, Switzerland
[2]Department of Orthopedics, Balgrist University Hospital Zurich, University of Zurich, Zurich, Switzerland
[3]Institute for Biomechanics, Swiss Federal Institute of Technology Zurich, Zurich, Switzerland

[a)]Author to whom correspondence should be addressed: apavlic@ethz.ch

ABSTRACT

Precise manipulation of fluids and objects on the microscale is seldom a simple task, but, nevertheless, crucial for many applications in life sciences and chemical engineering. We present a microfluidic chip fabricated in silicon–glass, featuring one or several pairs of acoustically excited sharp edges at side channels that drive a pumping flow throughout the chip and produce a strong mixing flow in their vicinity. The chip is simultaneously capable of focusing cells and microparticles that are suspended in the flow. The multifunctional micropump provides a continuous flow across a wide range of excitation frequencies (80 kHz–2 MHz), with flow rates ranging from nl min^{-1} to μl min^{-1}, depending on the excitation parameters. In the low-voltage regime, the flow rate depends quadratically on the voltage applied to the piezoelectric transducer, making the pump programmable. The behavior in the system is elucidated with finite element method simulations, which are in good agreement with experimentally observed behavior. The acoustic radiation force arising due to a fluidic channel resonance is responsible for the focusing of cells and microparticles, while the streaming produced by the pair of sharp edges generates the pumping and the mixing flow. If cell focusing is detrimental for a certain application, it can also be avoided by exciting the system away from the resonance frequency of the fluidic channel. The device, with its unique bundle of functionalities, displays great potential for various biochemical applications.

I. INTRODUCTION

Biomedical and chemical processes often require small amounts of biochemical substances, including cell and microparticle suspensions, to be moved around at the microscale with great precision.[1,2] There are various mechanisms that have been developed toward this objective, sometimes employing physical principles of piezoelectricity in combination with a diaphragm,[3] electrostatic[4] and electromagnetic[5] forces, thermal actuation,[6] bubble expansion and collapse,[7] electrowetting,[8] and acoustics,[9–15] among others. In view of the small amounts of sample and to minimize contamination, it is of great importance to combine as many processing steps as possible in a single lab-on-a-chip.

One particular way of enforcing the fluid motion in microfluidic systems is through a phenomenon called acoustic streaming.[16] This streaming is a steady fluid motion due to the attenuation of acoustic oscillations near a boundary[17,18] or in the bulk of the fluid,[19] but can also stem from a dynamic geometric nonlinearity.[20] A special form of the boundary-driven streaming is the streaming near sharp edges, which can be traced back to the acoustic needle experiments of Hughes and Nyborg[21] in 1962, for the disruption of cells. Since then, acoustically excited sharp edges have proven to be a promising technology for streaming-based mixing[22–29] and pumping[9,30] of fluids,[30] and even for acoustic-radiation-force-based trapping of particles and cells.[31,32] A series of recent studies revealed a general streaming flow pattern around a single sharp edge that features an outflowing vortex at the sharp tip, as shown in Fig. 1(a).[22–24,28,33] A recent review by Chen *et al.*[34] further describes the relevance and broad applicability of sharp-edge-based acoustofluidics.

In addition, the acoustic radiation force (ARF) is used for particle and cell trapping and focusing[35,36] as well as for the separation of particles, cells, and droplets.[37–39] A suitable ARF for such applications can

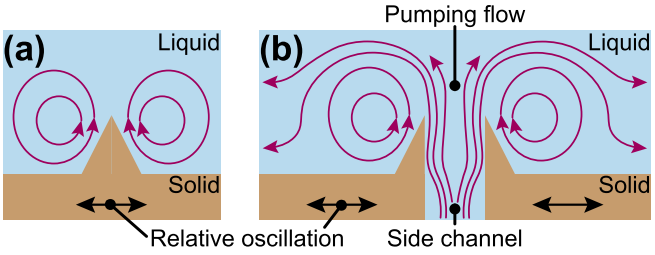

FIG. 1. Visualization of (a) the typical acoustic streaming flow around a single sharp edge that oscillates relative to the liquid, and of (b) the pumping mechanism driven by a pair of sharp edges at a side channel.

be achieved in different systems, one of which is the bulk acoustic wave (BAW) device.[40] When a BAW device is excited, the acoustic waves propagate throughout the whole device, forming standing waves when the frequency of excitation corresponds to a certain resonance mode of the fluidic channel or the whole device.[41,42]

Devices featuring such acoustic phenomena are recognized, for example, as a superior alternative to passive microreactors for chemical engineering.[43] However, one of the main challenges for the improvement of the technology was defined as constructing the acoustic microreactors from materials other than polydimethylsiloxane (PDMS) and lithium niobate, which would reduce the cost and production complexity while increasing the resistance to extreme reaction conditions.

Here, we present a silicon–glass chip which is driven by a pair of acoustically excited sharp edges and is simultaneously capable of fluid pumping and mixing, and of focusing and trapping of cells and microparticles in a suspension. The robust device provides a continuous flow across a wide range of excitation frequencies (80 kHz − 2 MHz), and programmable flow rates in the nl min^{-1} to μl min^{-1} range. The novel pumping mechanism featured in our device is based on a pair of sharp edges located at a side channel, pumping the liquid out of the side channel, as depicted in Fig. 1(b). Furthermore, in contrast to a low-frequency sharp-edge-based pump made of polydimethylsiloxane (PDMS) by Huang *et al.*,[9] where the solid edges oscillate and drive the flow, our device operates at higher frequencies that support resonances in the solid–liquid system. The resonances can boost the relative oscillatory velocity between sharp edges and the liquid, which is known to drive the streaming[28] and consequently the pumping. The behavior in the experimental system is explained through finite element method simulations. It is shown that the streaming around sharp edges drives the pumping and the mixing, while using a specific frequency can excite a standing wave in a part of the microfluidic device, leading to a simultaneous ARF-based focusing or trapping of cells and microparticles. Exciting the system at an off resonance frequency of the fluidic channel allows for the suppression of the focusing, thus allowing for the particles to remain dispersed in the pumping flow if desired.

A wide range of acoustofluidic phenomena can also be achieved with bubble-based devices, but the sharp-edge-based chip design is more robust and reliable, in particular for long-term use, as it avoids the instabilities associated with acoustically excited bubbles.[34] The silicon–glass composition makes our device chemically resistant, solving one of the challenges of acoustic microreactors for chemical engineering.[34,43,44] Furthermore, our device operates in a relatively broad frequency range, from 80 kHz to 2 MHz, enabling the control of acoustic cavitation, which is interesting for biomedical applications such as cell lysis.[45] The additional functionalities of our device—mixing, focusing, and trapping—make it attractive for various applications, such as boosting the sensitivity of bead-based immunoassays or bioassays,[46] trapping cells for medium exchange,[47] or improving cell isolation.[15]

II. THEORETICAL BACKGROUND

The motion of a viscous fluid is governed by the compressible Navier–Stokes equations

$$\rho\left[\frac{\partial \boldsymbol{v}}{\partial t} + (\boldsymbol{v}\cdot\boldsymbol{\nabla})\boldsymbol{v}\right] = -\boldsymbol{\nabla}p + \eta\boldsymbol{\nabla}^2\boldsymbol{v} + \left(\eta_B + \frac{\eta}{3}\right)\boldsymbol{\nabla}(\boldsymbol{\nabla}\cdot\boldsymbol{v}), \quad (1)$$

and the continuity equation

$$\frac{\partial \rho}{\partial t} = -\boldsymbol{\nabla}\cdot(\rho\boldsymbol{v}), \quad (2)$$

with the velocity $\boldsymbol{v}$, the dynamic viscosity η, and the bulk viscosity η_B. The density ρ is assumed to only be a function of the pressure p, namely,

$$\rho = \rho(p). \quad (3)$$

The equations are linearized using the regular perturbation approach.[48] Accordingly, the physical fields are expanded in a series, $\square = \square_0 + \square_1 + \square_2 + \cdots$, with $\square$ representing the field and the subscript representing the respective order.

A. First-order (acoustic) problem

For a quiescent fluid ($\boldsymbol{v}_0 = \boldsymbol{0}$), the substitution of the perturbed fields into the governing Eqs. (1) and (2) yields the following set of first-order equations:

$$\rho_0\frac{\partial \boldsymbol{v}_1}{\partial t} = -\boldsymbol{\nabla}p_1 + \eta\boldsymbol{\nabla}^2\boldsymbol{v}_1 + \left(\eta_B + \frac{\eta}{3}\right)\boldsymbol{\nabla}(\boldsymbol{\nabla}\cdot\boldsymbol{v}_1), \quad (4)$$

$$\frac{\partial \rho_1}{\partial t} = -\rho_0\boldsymbol{\nabla}\cdot\boldsymbol{v}_1, \quad (5)$$

with the equilibrium density ρ_0. The equation of state for the barotropic fluid

$$\rho_1 = \frac{1}{c_0^2}p_1 \quad (6)$$

is connecting the first-order density with the first-order pressure through the speed of sound in the fluid c_0. The first-order fields are assumed to have a harmonic time-dependency with $e^{i\omega t}$, where $\omega = 2\pi f$, defined by the frequency f.

B. Second-order (streaming) problem

Applying the perturbation theory up to second order to the governing equations, namely,

$$\rho_0\frac{\partial \boldsymbol{v}_2}{\partial t} - \left(\eta_B + \frac{\eta}{3}\right)\boldsymbol{\nabla}(\boldsymbol{\nabla}\boldsymbol{v}_2) + \boldsymbol{\nabla}p_2 - \eta\boldsymbol{\nabla}^2\boldsymbol{v}_2 = -\rho_0(\boldsymbol{v}_1\cdot\boldsymbol{\nabla})\boldsymbol{v}_1 - \rho_1\frac{\partial \boldsymbol{v}_1}{\partial t} \quad (7)$$

and

$$\frac{\partial \rho_2}{\partial t} + \rho_0 \nabla \cdot \boldsymbol{v}_2 = -\rho_1 \nabla \cdot \boldsymbol{v}_1 \tag{8}$$

together with taking the time average $\langle \square \rangle = \frac{1}{T}\int_T \square \mathrm{d}t$ over an oscillation period T, results in the equations of acoustic streaming,[16,49]

$$\nabla \langle p_2 \rangle - \eta \nabla^2 \langle \boldsymbol{v}_2 \rangle - \left(\eta_B + \frac{\eta}{3}\right) \nabla (\nabla \cdot \langle \boldsymbol{v}_2 \rangle) = -\rho_0 \nabla \cdot \langle \boldsymbol{v}_1 \boldsymbol{v}_1 \rangle, \tag{9}$$

$$\rho_0 \nabla \cdot \langle \boldsymbol{v}_2 \rangle = -\nabla \cdot \langle \rho_1 \boldsymbol{v}_1 \rangle. \tag{10}$$

At the second order, the no-slip boundary condition is imposed on the Lagrangian fluid velocity at the fluid–solid interface, to account for the oscillations of the interface at the first order. The Lagrangian velocity is defined as the summation of the Eulerian streaming velocity $\langle \boldsymbol{v}_2 \rangle$ and the Stokes drift,[50,51]

$$\boldsymbol{v}_{SD} = \left\langle \left(\int \boldsymbol{v}_1 \mathrm{d}t \cdot \nabla \right) \boldsymbol{v}_1 \right\rangle. \tag{11}$$

The boundary condition consequently translates into

$$\langle \boldsymbol{v}_2 \rangle = -\boldsymbol{v}_{SD} \quad \text{at the interface.} \tag{12}$$

However, $\boldsymbol{v}_{SD} = \boldsymbol{0}$ at the boundaries that are rigid.

C. Acoustic radiation force (ARF)

When an acoustic wave inside an acoustofluidic device scatters at an object such as a microparticle or a cell, it gives rise to the acoustic radiation force (ARF). The ARF results from the interactions between the scattered and the background acoustic waves. When an inviscid fluid and a spherical object can be assumed, which is often the case, the ARF can be approximated as the negative gradient of the Gor'kov potential,[52] namely,

$$\boldsymbol{F}_{rad} = -\nabla U, \tag{13}$$

where the Gor'kov potential can be written as

$$U = \frac{4}{3}\pi a^3 \left(\frac{1}{2} \frac{f_1}{c_0^2 \rho_0} \langle p_1^{bg} p_1^{bg} \rangle - \frac{3}{4} \rho_0 f_2 \langle \boldsymbol{v}_1^{bg} \cdot \boldsymbol{v}_1^{bg} \rangle \right), \tag{14}$$

with the object's radius being a, the background acoustic pressure p_1^{bg}, the background acoustic velocity $\boldsymbol{v}_1^{bg}$, and the monopole and the dipole scattering coefficients f_1 and f_2, respectively. This formulation is applicable under the assumption that the object is small compared to the acoustic wavelength and far away from the walls. However, a recent study[53] showed that the Gor'kov potential is in most cases valid even in close proximity to a wall.

When considering a one-dimensional plane standing wave along a z-axis, the ARF from Eq. (13) further simplifies to

$$\boldsymbol{F}_{rad}^{1D} = 4\pi a^3 \Phi k E_{ac} \sin(2kz) \boldsymbol{e}_z, \tag{15}$$

with the acoustic energy density $E_{ac} = p_a^2/(4\rho_0 c_0^2)$, the pressure amplitude p_a, the ideal wave number $k = \omega/c_0$, and the unit vector $\boldsymbol{e}_z$ oriented along the z-axis. Equation (15) is attributed to Yosioka and Kawasima.[54] The acoustic properties of the object relative to the fluid are condensed into the acoustic contrast factor

$$\Phi = \frac{1}{3} f_1 + \frac{1}{2} f_2 = \frac{1}{3} \left[\frac{5\tilde{\rho} - 2}{2\tilde{\rho} + 1} - \tilde{\kappa} \right], \tag{16}$$

in which the relative compressibility $\tilde{\kappa} = \kappa_{obj}/\kappa_0$ and density $\tilde{\rho} = \rho_{obj}/\rho_0$ reflect the ratios between the properties of the object $\square_{obj}$ and the fluid $\square_0$.

III. MATERIALS AND METHODS

A. Devices and fabrication

The lab-on-a-chip devices shown in Fig. 2 were produced through cleanroom processing and feature a two-layered structure made of silicon and glass. The channel designs were first patterned on a silicon wafer (500 ± 10 μm thickness) through photolithography (resist: S1828/S1818, Shipley, 4000 rpm; developer: AZ351B, Microchemicals) and then etched with an inductively coupled plasma deep reactive ion etching (ICP-DRIE) machine (Estrellas, Oxford Instruments) to a depth of ∼184 μm.

Afterward, a glass wafer (500 μm thickness) was anodically bonded onto the silicon wafer. The wafer was then diced into individual 12 × 24 mm^2 chips with a wafer saw (DAD3221, Disco Corporation). Fused silica capillaries (164±6 μm outer diameter, 100±6 μm inner diameter, Molex) were inserted into the inlets and outlets of the chips and fixed with a two-component glue (5 min Epoxy, Devcon). A piezoelectric transducer (PZT) (length × width × thickness = 10 × 2 × 1 or 16.75 × 8.74 × 17.4 mm^3, Pz26, Meggitt Ferroperm) was glued to the backside of each device with a conductive epoxy (H20E, EPO-TEK). Copper cables (0.15 mm diameter) were connected to the PZT using a conductive silver paste and glued to a device with instant glue for mechanical stability.

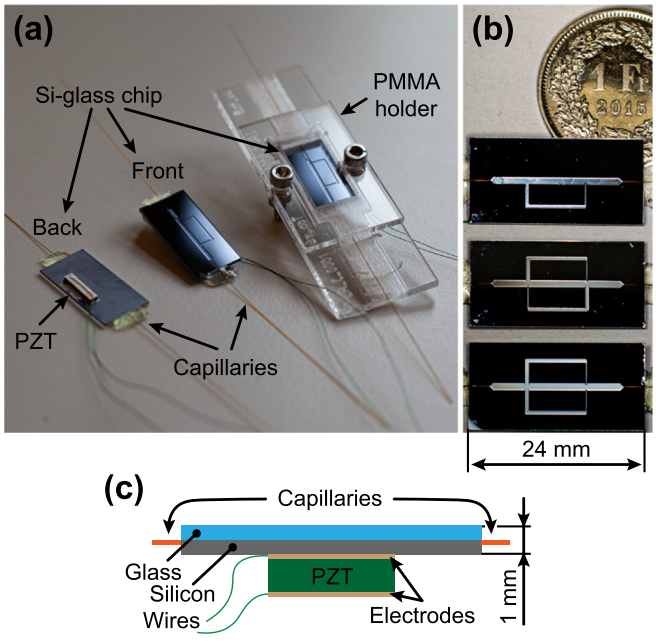

FIG. 2. (a) Experimental device, featuring a silicon–glass chip, piezoelectric transducer (PZT), holder from acrylic glass (PMMA), and connections made out of fused silica capillaries. (b) Three different device designs that are featured in the manuscript next to a one Swiss franc coin for scale. (c) The schematic cross section of a device, explaining individual layers. The size of an individual silicon–glass chip without supporting elements is 1 × 12 × 24 mm^3.

To fix the devices under the microscope, a chip-holder was designed and laser-cut from acrylic glass (PMMA), with top and bottom parts being held together by two bolts, as depicted in Fig. 2(a).

The devices were designed to have a 1 mm wide main channel across the length of the device, to which one or two loops of side channels are connected, as visible in Fig. 2(b). An example of a single side channel loop device is shown in Fig. 3. The default width of side channels is 500 μm, except for side channel segments that start with a pair of sharp edges, for which the width varies between 100 and 500 μm. The width of this side channel segment is equal to the spacing between the pair of sharp edges and is specified for each device alongside the corresponding results. All sharp edges in the study feature a 10° apex angle and are oriented, such that one of the sides of the edge is aligned with a wall of the adjacent side channel. Measurements of the geometry of devices at the end of the production revealed the rounding radius of the sharp edges of ∼0.9 μm, the apex angle of a sharp edge of ∼10.3°, the length of the protrusion of sharp edges into the main channel of ∼275 μm, and the deviation of channel widths on the order of <1%.

B. Experimental setup

For visual observation of phenomena within the channels of the lab-on-a-chip devices, we used a microscope (Axioscope, Zeiss) with a blue LED (COP4-A, Thorlabs) and a high-speed camera (HiSpec1 2G Mono, Fastec Imaging). To visualize the flow field and demonstrate the acoustic forces, yeast cells (Coop Supermarket) and polystyrene (PS) beads (5.19 ± 0.14 μm, microParticles GmbH) were used. Pressure pumps (Flow EZ, Fluigent) were connected to the inlet capillaries of a device, for supplying the particles/cells dispersed in water as well as for re-dispersing the particles/cells within the chip in-between experiments. A function generator (Model DS345, Stanford Research Systems) and an amplifier (HSA 4101, NF Corporation) were used to drive the PZT and monitored through an oscilloscope (Model 9410, LeCroy).

Devices were characterized by measuring the admittance of the PZT with an impedance analyzer (Sine Phase Z-Check 16777k) as reported in the supplementary material.

The pumping velocity was estimated through manual particle tracking velocimetry (Fiji[55]) of the PS particles. The flow rate was computed by assuming that the flow profile corresponds to the Poiseuille flow through a rectangular cross section,[56] and that the velocity measured in the middle of the channel corresponds to the maximal velocity of the flow profile. The trajectories of PS particles that were used for estimation of the acoustic pressure amplitude (p_a) were obtained through a particle tracking velocimetry plugin TrackMate[57] in Fiji[55] and postprocessed with a custom Matlab[58] code (described in the supplementary material).

The time-averaged paths of PS particles through the system were obtained by applying the variance mode to a stack of several video frames in Adobe Photoshop.

C. Numerical model

The numerical model resembling the region of interest (ROI) of one of the devices, as indicated in Fig. 3(c), was based on a finite element method framework of COMSOL Multiphysics v. 5.6.[59] The geometry with all the relevant dimensions and the applied boundary conditions are shown in Figs. 3(a) and 3(b). We only modeled the fluid domain in 2D, represented by the blue colored region in Figs. 3(a) and 3(b), taking the walls as rigid boundaries. The material properties used for the modeling are given in Table I.

The perturbation approach presented in Sec. II was used for the numerical modeling, similarly to previous studies.[61] The fluid domain is excited through boundary conditions specified in Fig. 3(a), by applying a zero acoustic pressure at the left-hand side boundary of the main channel, and an oscillatory velocity with an amplitude of v_a along the

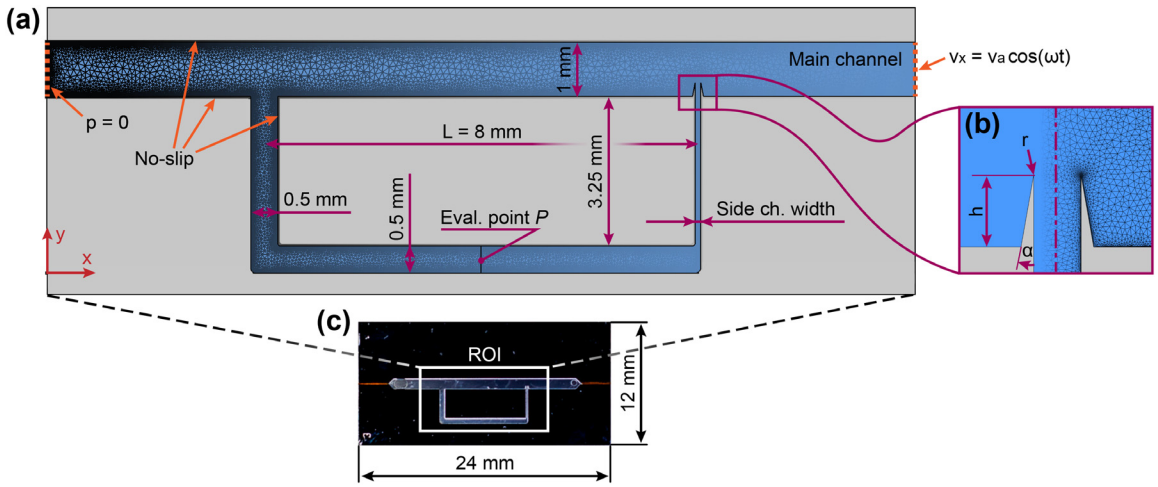

FIG. 3. (a) Geometry and mesh used in the numerical simulations, with the description of geometrical parameters and boundary conditions applied in the numerical model. The blue region corresponds to the modeled fluid domain, whereas the gray area represents the solid structure of the device, which we assume to be rigid. (b) Detailed view of the geometry of sharp edges, with a refined mesh at the tips of sharp edges and at boundaries. The parameters that define the geometry of the sharp edge pair are the height of the sharp edges h, the angle of each sharp edge α, and the rounding radius of the edges r. (c) Region of interest on an actual device that corresponds to the numerical model. The size of the chip in (c) is 12 × 24 mm^2.

TABLE I. The material parameters for water (H_2O) and polystyrene[60] (PS). The solid elastic polystyrene is defined through the speed of primary and secondary waves, c_{obj}^P and c_{obj}^S, respectively. The acoustic contrast factor Φ is computed using $\kappa_{obj} = 1/(\rho_P[(c_{obj}^P)^2 - \frac{4}{3}(c_{obj}^S)^2])$.

	H_2O	Unit		PS	Unit
ρ_0	1000	$kg\,m^{-3}$	ρ_{obj}	1050	$kg\,m^{-3}$
c_0	1481	$m\,s^{-1}$	c_{obj}^P	2400	$m\,s^{-1}$
η	1.002	mPa s	c_{obj}^S	1150	$m\,s^{-1}$
η_B	3.09	mPa s	Φ	0.175	—

x-direction at the right-hand side boundary of the main channel. The rounding of the sharp edges is defined through the viscous boundary layer as $r = \delta/10$, which ensures that the resulting streaming is independent of r, as demonstrated by Zhang *et al.*[24] The detailed description of the numerical model is given in the supplementary material.

IV. RESULTS

The investigated device features various functionalities that are graphically summarized in Fig. 4. The main two are the pumping flow due to a single pair of sharp edges and the focusing of cells and microparticles due to the ARF in a standing acoustic wave. Other functionalities that are demonstrated in the manuscript are trapping of cells with the localized pressure nodes in the side channels, and fluid mixing due to the strong acoustic streaming field near the two sharp edges. The results that demonstrate and characterize these functionalities are further discussed in Secs. IV A and IV B.

A. Pumping and mixing

The pumping flow is demonstrated in Fig. 5(a) (Multimedia view) through the time-averaged paths of 5.19 μm diameter PS particles in water. Near the two sharp edges, the particles follow the streamlines of the vortices that are typical around sharp edges[28] and that are usable for mixing[25–27] at the microscale. The pumping flow in the counterclockwise direction, which results from the streaming around the two sharp edges,[9] moves the particles from the mixing to the focusing region, and then back to the mixing region by pumping the particles through the side channel. The sharp edge angles of ~10° are employed to maximize the streaming velocity, since it has been

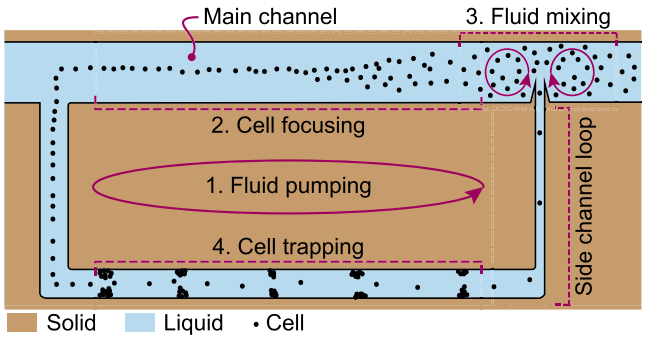

FIG. 4. Overview of the four main functionalities of the device. (1) Fluid pumping, (2) cell/microparticle focusing, (3) fluid mixing, and (4) cell/microparticle trapping.

shown by Zhang *et al.*[24] and Doinikov *et al.*[28] that the sharper the angle, the higher the streaming velocity at a fixed amplitude of the first-order excitation velocity.

The behavior corresponding to the device from Fig. 5(a) is analyzed with the help of the numerical model. The resulting acoustic pressure field is shown through colors in Fig. 5(c), indicating that the pressure nodal plane appears near the middle of the main channel, at the frequency of 746 kHz. This frequency is lower than in an experimental setting [Fig. 5(a)] due to simplifying the problem to two dimensions, and assuming rigid walls, both of which can influence the resonance frequency. The Gor'kov potential (color) and the ARF (arrows) in the focusing region are shown in Fig. 5(d) and confirm that the PS particles are being forced to the middle of the channel. Furthermore, the simulation of the Eulerian acoustic streaming, the streamlines of which overlay the pressure field in Fig. 5(c), indicates the pumping flow as well as the mixing flow close to the two edges. Qualitatively, our simplified two-dimensional numerical rigid-wall model that is based on the regular perturbation technique[28,48] captures the observed pumping and mixing phenomena very well. However, the approach and the solution for the streaming velocity might be questionable in the proximity of the sharp tips, due to high velocities that can develop at those nearly singular points.[33] In order to improve the accuracy in that region, more sophisticated techniques would have to be applied, such as the direct numerical simulations (DNS)[24,33] or the analytical approaches suitable for the so-called fast streaming.[62] It is important to note that the region of concern near the sharp tips has a characteristic length on the order of the viscous boundary layer thickness $\delta = \sqrt{\eta/(\pi\rho_0 f)} = 0.63\ \mu$m at $f = 802$ kHz in water.

In the device from Fig. 5, we measured the flow rate in dependence of the applied voltage squared, at $f = 802$ kHz, as shown in Fig. 6. Specifically, we measured the velocity of the 5.19 μm PS particles in the pumping flow in the middle of the side channel that is parallel to the main channel, and transformed this velocity to the flow rate of a Poiseuille flow through the rectangular cross section of the channel. At the applied voltages of below $V_{pp} = 10$ V, the good linear fit in the region "A" of Fig. 6 corresponds to the expected linear relation between the streaming velocity and the applied voltage squared. However, between $V_{pp} = 10$ and 22 V, in the region "B," the slope of the fitted linear curve is steeper, indicating a relative boost of the streaming velocity and a nonlinear dependence of the streaming velocity on the applied voltage squared. Interestingly, this is the opposite behavior to that commonly observed in the streaming around sharp edges; for a single sharp edge, the slope of the increase in the streaming velocity with the increase in the applied voltage squared would start decreasing after a certain threshold amplitude is reached.[24,33] There is another regime, at above $V_{pp} = 22$ V—the region "C" in Fig. 6, where the streaming velocity is more or less independent of the applied voltage. The observed nonlinear behavior could indicate various physical mechanisms at play, such as the fluid turbulence, the maximal particle velocity threshold in the solid,[63] or nonlinearities associated with the piezoelectric transducer and the conductive epoxy layer connecting the transducer to the device.

The source of the deviation from the linear relation between the streaming velocity magnitude and the applied voltage squared, in the case of the sharp edge streaming, is not generally understood. As pointed out by Ovchinnikov *et al.*,[33] the nonlinearity could come from the increased influence of the third-order inertial term $(\langle \boldsymbol{v}_2 \rangle \cdot \boldsymbol{\nabla})\boldsymbol{v}_1$

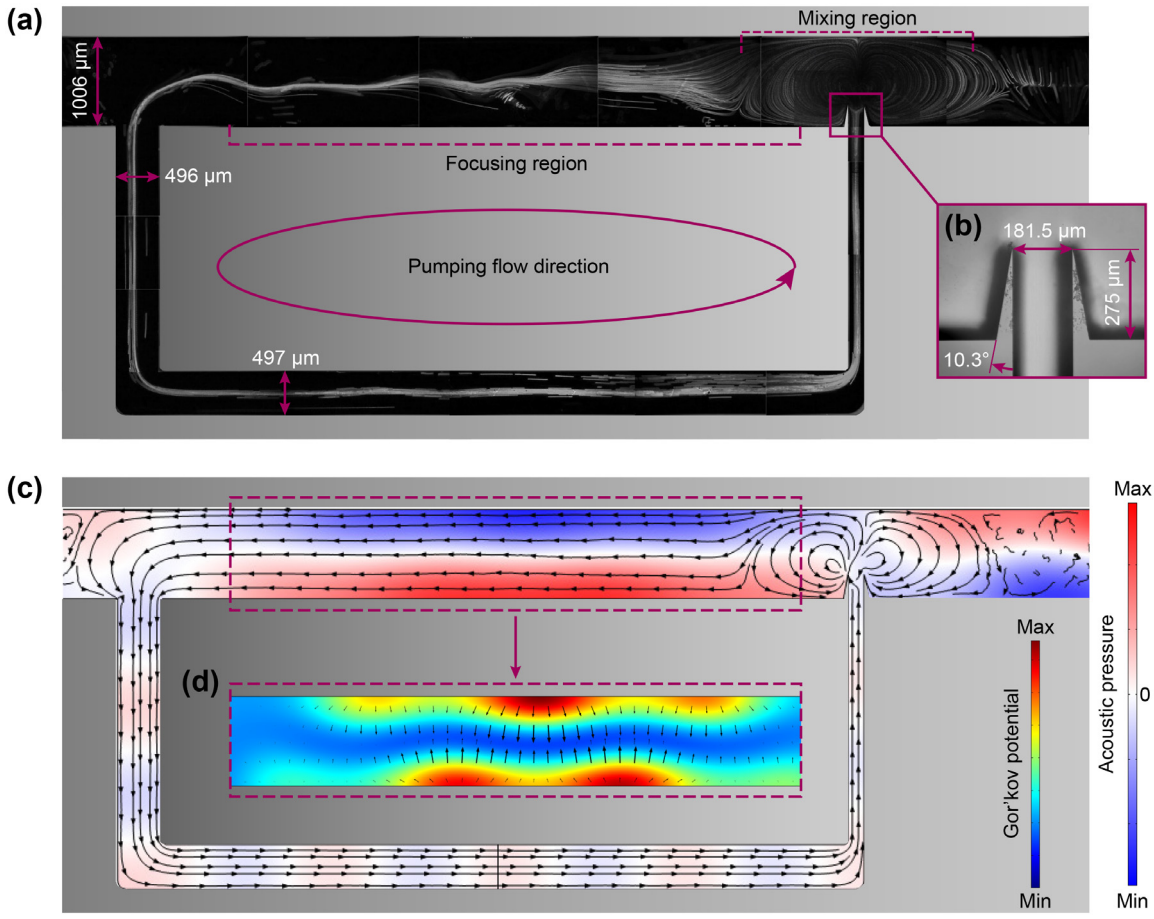

FIG. 5. (a) Time-averaged paths of 5.19 μm polystyrene particles in the experimental device that is excited at $f = 802$ kHz with 22 V_{pp}. The particles reveal the mixing around the two sharp edges, the focusing in the central region of the main channel, and the pumping through the main and side channel. Dimensions in (a) and (b) correspond to the measurements on the experimental device, yielding the spacing between the two edges of 181.5 μm. (c) Numerically, we found a matching streaming field and an acoustic pressure field that yields the pressure node at the middle of the main channel, at $f = 746$ kHz. In the model, the spacing between the two edges was adjusted to 180 μm, to match it to the spacing of the experimental device from (a). To avoid influence of effects near the ends of the main channel, the numerical model extends past the region that is shown here that matches the region from (a), observed in experiments. (d) The Gor'kov potential and the acoustic radiation force (arrows) further justify the focusing of the polystyrene particles at the pressure node. The time-averaged paths of PS particles through the system were obtained by applying the variance mode to a stack of several video frames in Adobe Photoshop. The direction of the experimentally observed flow near the sharp edges in (a) matches the direction of the numerically predicted streaming in (c). Multimedia view: https://doi.org/10.1063/5.0133992.1

that is neglected in the second-order momentum conservation Eq. (9), or from the interference of the streaming vortices with the surrounding geometry, according to Zhang *et al.*[24] Furthermore, the rounding radius of the sharp edges r was measured to be $\sim$0.9 μm, which is comparable to the viscous boundary layer thickness in the investigated range ($\delta \approx 0.56\,\mu$m at $f = 1$ MHz in water), and could be affecting the streaming flow. Doinikov *et al.*[28] derived a theoretical relation between the streaming velocity near a sharp edge and r, whereas Zhang *et al.*[24] showed numerically that the streaming velocity decreases as r increases, at $r > \delta$.

The flow rate in our devices reaches up to 4.1 μl min^{-1} at $V_{pp} = 28$ V and $f = 802$ kHz, which corresponds to the pumping pressure of $\sim$12 Pa, approximated through the Hagen–Poiseuille law,[56] considering the whole side channel loop. This is in the same order as the maximal flow rate and the pumping pressure generated in the previously reported PDMS acoustic sharp-edge micropump at $V_{pp} = 50$ V and $f = 6.5$ kHz, namely, $\sim$8 μl min^{-1} and $\sim$76 Pa; however, we use a single pair of sharp edges, whereas the PDMS device features 20 sharp edges.

To demonstrate a wide range of operating frequencies that can be used to operate our micropumping mechanism, we used a larger PZT ($16.75 \times 8.74 \times 17.4$ mm^3) that has a resonance frequency in the thickness direction at $\sim$80 kHz (based on the admittance analysis in the supplementary material). The maximal flow rate observed at $f = 78.26$ kHz, for the same voltage range as in Fig. 6, was 4.46 μl min^{-1} at $V_{pp} = 35$ V. This demonstrates the ability of driving the fluid pumping at frequencies that do not correspond to the resonances of the fluidic channel, which results in the pumping and mixing of the fluid without focusing cells/microparticles, as illustrated in Fig. 7(a) (Multimedia view).

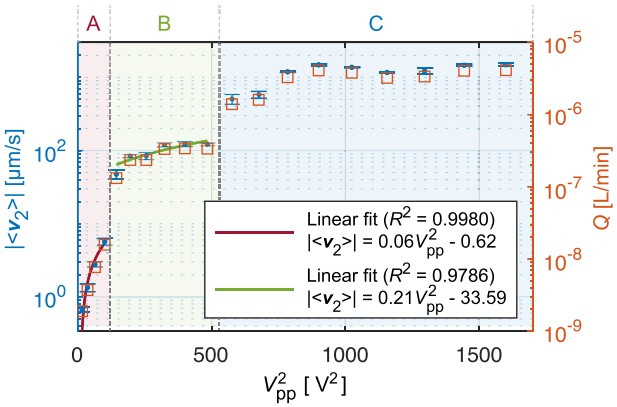

FIG. 6. Velocity of the pumping flow in the middle of the side channel parallel to the main channel (equivalent to the evaluation point *P* in Fig. 3), in dependence of the applied voltage squared. The device corresponds to the one in Fig. 5 as well as the frequency at $f = 802$ kHz. The graph is split into regions A, demonstrating a linear relationship between the streaming velocity and applied voltage squared, B, demonstrating the same linear relationship as in A but with a decreased slope, and C, a region where the streaming velocity cannot be increased by increasing the applied voltage squared, indicating a dominant influence of an unknown nonlinear physical mechanism.

Since the rate of the sharp edge pumping flow is controlled independently of the general flow through the whole device, which we control with the external pressure pump, we can fine-tune the flow rate in any of the side channel loops, and even bring it to stagnation, as illustrated in Fig. 7(b) (Multimedia view). This could potentially help increase the speed of operations like medium exchange or addition of a new sample, as the reduced flow in the side channel, while the PZT is excited, could impede the flushing of the trapped cells due to shear forces. The novelty of the device, therefore, lies in, but is not limited to, the programmable multifunctionality of the device, where each feature can either be used, in an arbitrary order, individually or simultaneously.

We also observed a dependence of the pumping flow on the spacing between the two edges. The pumping flows in the devices with two side channel loops in Fig. 8 (Multimedia view), with two pairs of sharp edges per loop, indicate that the narrower 100 μm spacing between the sharp edges generates a stronger pumping flow than the 500 μm spacing, when other conditions (e.g., V_{pp}, f, PZT placement, glue layer thickness, etc.) are kept constant. For each loop in Fig. 8, one of the sharp-edge pairs has a spacing of 100 μm, while the spacing is 500 μm for the other. Both ends of a side channel loop should facilitate the pumping, as was verified through two additional devices featuring a single side channel loop [same design as in Fig. 5(a)], with the spacing between the two edges of 100 μm and 500 μm, respectively. However, based on the observed flow directions (Fig. 8), the pumping from the sharp-edge pair with the narrower spacing prevails.

The streaming vortices around the sharp edges that are analogous to ours and that are responsible for the fluid mixing have been investigated extensively,[22–24,28,33] which is why we omit a detailed analysis on the subject.

B. Focusing and trapping of cells and microparticles

Objects of positive acoustic contrast ($\Phi > 0$) are, in accordance with Eq. (15), forced toward pressure nodes of a one-dimensional

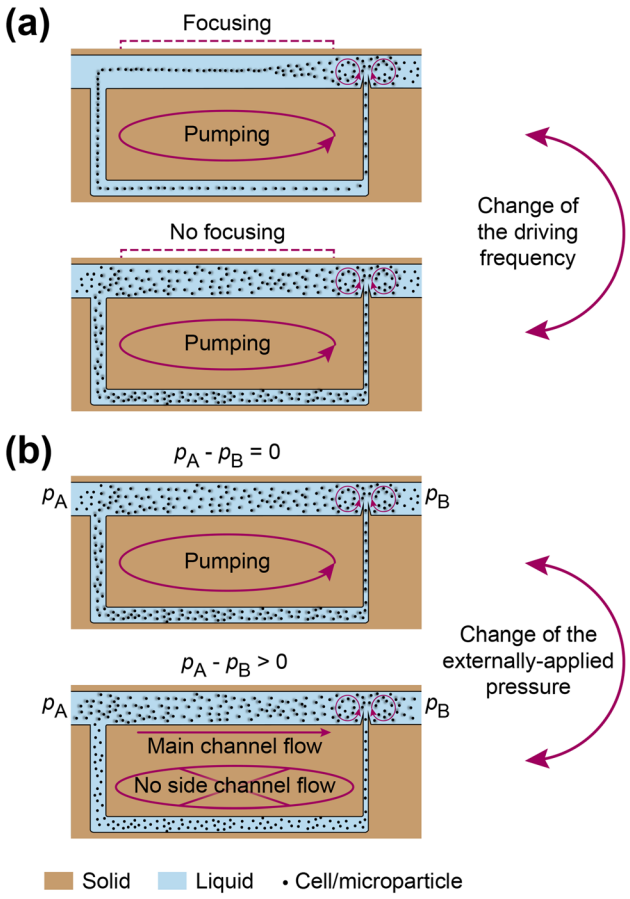

FIG. 7. (a) When the device is excited at a resonance frequency of the main channel, a pumping and mixing flow can be achieved in combination with particle focusing as demonstrated in Fig. 5. When the frequency is shifted away from the resonance frequency of the fluid channel, the pumping and mixing flows can persist in the absence of the focusing of cells or microparticles. (b) Applying a pressure difference with an external pressure pump and, thus, inducing an additional flow through the main channel of the device while simultaneously exciting the device acoustically can suppress the flow in the side channel loop. Multimedia views: https://doi.org/10.1063/5.0133992.2; https://doi.org/10.1063/5.0133992.3

standing wave. This links the PS particles being focused toward the middle of the main channel in Fig. 5(a) and the simulated acoustic pressure in Fig. 5(c) indicating the pressure nodal line in the focusing region. The Gor'kov potential (color) and the ARF (arrows) in Fig. 5(d) further confirm that the PS particles are forced toward the middle of the main channel.

The hard silicon walls of our devices provide a strong acoustic impedance mismatch with respect to water, 19.79×10^6 kg m^{-2} s^{-1} compared to 1.49×10^6 kg m^{-2} s^{-1}, leading to the acoustically hard wall boundary condition for water at the solid–fluid interface ($v_1 \approx 0$ at the interface) being a good model.[64] This can result in a quasi one-dimensional standing wave between the walls of the main channel, featuring a $n\lambda/2$ ultrasound resonance mode, where $n = 1, 2, 3, \ldots$ represents an individual resonance mode and $\lambda = c_0/f$ the acoustic wavelength.[48] For a fixed channel width, the resonance mode that is

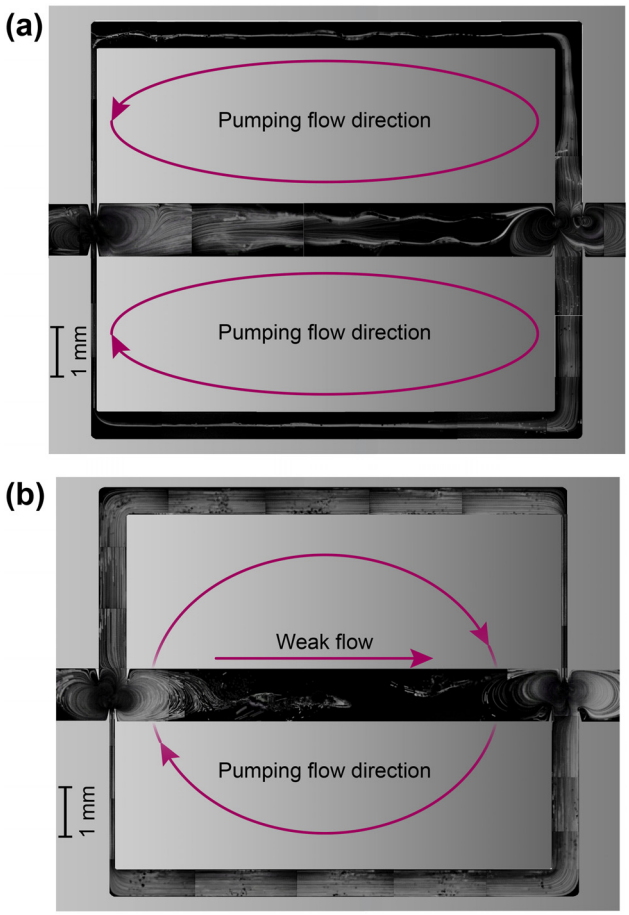

FIG. 8. Time-averaged paths of 5.19 μm polystyrene particles in devices that feature two side channel loops with four pairs of sharp edges, with spacing between the two edges of 100 or 500 μm. The width of the main channel of the two devices is 1 mm. (a) Pairs of sharp edges with equal spacing between the two edges are opposing each other (100 μm on the left and 500 μm on the right). The device was excited at $f = 1.371$ MHz with $V_{pp} = 30$ V. (b) Pairs of different spacing between the two edges are opposing each other (100 μm bottom left and top right, 500 μm top left and bottom right). The device was excited at $f = 780$ kHz with $V_{pp} = 6$ V. The arrows show the direction of the pumping flow, while the time-averaged paths of polystyrene particles reveal regions of focusing in (a) that appear as thin bright lines in the channels and a uniform flow in (b). The weak flow in the main channel in (b) is a result of a slight imbalance between the pumping strength of equally spaced sharp edge pairs, which is likely due to the spatial variability of the oscillatory velocity of the sharp edges relative to the liquid. The time-averaged paths of PS particles through the system were obtained by applying the variance mode to a stack of several video frames in Adobe Photoshop. Multimedia views: https://doi.org/10.1063/5.0133992.4; https://doi.org/10.1063/5.0133992.5

excited depends on the frequency of excitation: the $\lambda/2$ mode, with its single pressure nodal plane, is visible at $f = 802$ kHz in the 1 mm wide main channel in Fig. 5(a), and at $f = 1.371$ MHz in the 0.5 mm wide side channels in Fig. 8(a). The λ resonance mode, featuring two pressure nodal lines, was observed at $f = 1.371$ MHz in the 1 mm wide main channel in Fig. 8(a).

The acoustic pressure amplitude was measured in the region of the main channel outside the loop, where the mixing and pumping streaming flows were not evident (see the supplementary material for details). The resulting average pressure amplitude $p_a = 1.2$ MPa corresponds to $E_{ac} = 160$ J m^{-3}, which is in the typical range for silicon–glass chips,[65] considering the $V_{pp} = 22$ V excitation.

In addition to the one-dimensional standing waves perpendicular to the channel mentioned so far, other resonance modes can be excited inside a device, yielding interesting trapping regions. Figure 9 (Multimedia view) shows clusters of trapped yeast cells in the side channel loop, showcasing the $n = 4$ resonance mode in the two channels perpendicular to the main channel and the $n = 8$ mode along the channel parallel to the main channel, while also yielding the $n = 1$ mode across the main channel, with a single pressure nodal line. The trapped cells in Fig. 9 are disconnected across the channel width in the side channel loop due to the pumping flow that features the highest velocity in the middle of the channel cross section and obstructs the trapping.

Such trapping capabilities, in combination with the flow control through the side channel, could improve the efficiency of the cell isolation process[15] or the medium exchange.[47] The acoustic radiation force that is the mechanism behind the trapping and focusing in our device scales with the volume of a cell, whereas the drag force from the acoustic streaming scales with the radius of the cell. Consequently, fine-tuning the flow rate through the side channel loop and the strength of the trapping, by modifying the voltage applied to the PZT and the external pressure difference applied to the main channel, could lead to size-selective separation of cells, with a programmable size threshold.

Past viability studies suggest that the acoustic energy densities needed for the trapping and focusing of cells do not harm the cells directly.[45] The damage could occur through the heating of the device, which is analyzed in the supplementary material and can be controlled with an external system.[66] A second mechanism for cell damage could be cavitation, which is minimized by the use of high frequencies and low p_a. In our system, local shear forces due to the sharp-edge streaming present an additional mechanism that could potentially damage cells, which was recently investigated by Wang *et al.*[67]

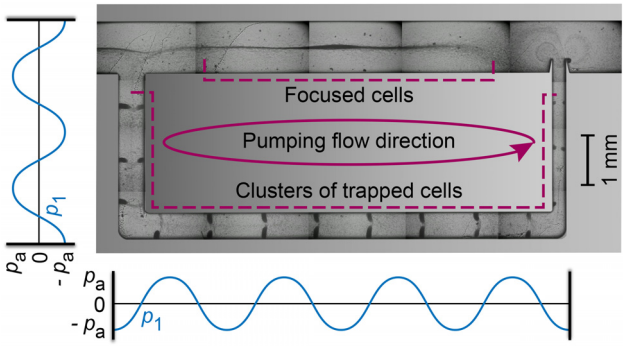

FIG. 9. Trapping and focusing of yeast cells in water, demonstrated using a device featuring a 260 μm spacing between the two sharp edges, and is otherwise equal to the device from Fig. 5, with 1 mm wide main channel. The image is a mosaic of several snapshots of channel segments, taken while the device was being excited at $f = 714$ kHz with $V_{RMS} = 30$ V. The dark spots in the channel are the trapped clusters of yeast. The direction of the pumping flow is indicated by the arrow. The illustrated quasi-one-dimensional pressure fields along the side channels indicate the corresponding $n = 4$ and 8 resonance modes that focus and trap the yeast cells. Multimedia view: https://doi.org/10.1063/5.0133992.6

V. CONCLUSIONS

The presented microfluidic chip offers a platform that is especially relevant for applications where multiple functions are needed within the same chip, particularly pumping, mixing, and focusing or trapping of cells and microparticles. We demonstrated a continuous pumping in the range of excitation frequencies from 80 kHz to above 1 MHz, with the corresponding programmable flow rates of up to $\sim 4\,\mu l\,min^{-1}$ ($\sim$12 Pa pumping pressure). The pumping is always paired with the mixing vortices near the sharp edges that drive the pumping flow. We also demonstrated the focusing and trapping capabilities of our device by predicting and observing the behavior of polystyrene microparticles and yeast cells in combination with different resonance modes of the fluidic channels. Our silicon–glass device is chemically resistant, solving one of the main problems of acoustic microreactors for chemical engineering.[34,43] The pumping and strong mixing at the sharp edges could provide a tool for cell disruption, similar to what Hughes and Nyborg[21] demonstrated, but with the ability to disrupt larger samples in a very controlled manner. The unique precisely programmable multifunctionality that the device can provide could also be beneficial in studying the dynamics of active matter, such as bacteria[68] or Janus particles.[69] Furthermore, it has been previously demonstrated that imposing a standing acoustic wave can significantly improve the sensitivity of particle-based immunoassays.[46] The combination of mixing, focusing, and pumping that our device provides could lead to an even higher sensitivity of these methods.

In the future, the device design will be further optimized based on the needs of specific applications. The process will be aided by the presented numerical model that is capable of predicting the acoustofluidic phenomena inside such lab-on-a-chip devices. Furthermore, to make the device compatible with imaging techniques that require a transparent substrate, such as inverted microscopy and phase contrast microscopy, a see-through version of the presented device could be realized by bonding an additional glass wafer to the silicon wafer prior to the described device production process, and then etching through the whole silicon layer, as done by Harshbarger *et al.*[70]

SUPPLEMENTARY MATERIAL

See the supplementary material for details on the numerical model, admittance analysis, details on measuring the acoustic pressure amplitude, and temperature measurement.

AUTHOR DECLARATIONS

Conflict of Interest

The authors have no conflicts to disclose.

Author Contributions

Alen Pavlic: Conceptualization (lead); Data curation (lead); Formal analysis (lead); Investigation (equal); Methodology (lead); Project administration (lead); Software (lead); Supervision (equal); Validation (equal); Visualization (lead); Writing – original draft (lead); Writing – review & editing (equal). **Cooper Lars Harshbarger:** Conceptualization (supporting); Investigation (supporting); Methodology (supporting); Project administration (supporting); Supervision (equal); Validation (supporting); Writing – original draft (supporting); Writing – review & editing (equal). **Luca Rosenthaler:** Conceptualization (supporting); Data curation (supporting); Investigation (equal); Methodology (supporting); Validation (supporting); Writing – review & editing (supporting). **Jess Gerrit Snedeker:** Conceptualization (supporting); Funding acquisition (supporting); Resources (supporting); Supervision (supporting); Writing – review & editing (supporting). **Jürg Dual:** Conceptualization (supporting); Funding acquisition (lead); Methodology (supporting); Project administration (supporting); Resources (lead); Supervision (supporting); Writing – review & editing (supporting).

DATA AVAILABILITY

The data that support the findings of this study are available from the corresponding author upon reasonable request.

REFERENCES

[1] Y.-N. Wang and L.-M. Fu, "Micropumps and biomedical applications—A review," Microelectron. Eng. **195**, 121–138 (2018).
[2] C. K. Byun, K. Abi-Samra, Y.-K. Cho, and S. Takayama, "Pumps for microfluidic cell culture," Electrophoresis **35**, 245–257 (2014).
[3] H. A. Dereshgi, H. Dal, and M. Z. Yildiz, "Piezoelectric micropumps: State of the art review," Microsyst. Technol. **27**, 4127–4155 (2021).
[4] H. Kim, A. A. Astle, K. Najafi, L. P. Bernal, and P. D. Washabaugh, "An integrated electrostatic peristaltic 18-stage gas micropump with active microvalves," J. Microelectromech. Syst. **24**, 192–206 (2014).
[5] M. Rusli, P. S. Chee, R. Arsat, K. X. Lau, and P. L. Leow, "Electromagnetic actuation dual-chamber bidirectional flow micropump," Sens. Actuators, A **282**, 17–27 (2018).
[6] N. A. Hamid, B. Y. Majlis, J. Yunas, A. Syafeeza, Y. C. Wong, and M. Ibrahim, "A stack bonded thermo-pneumatic micro-pump utilizing polyimide based actuator membrane for biomedical applications," Microsyst. Technol. **23**, 4037–4043 (2017).
[7] A. Oskooei and A. Günther, "Bubble pump: Scalable strategy for in-plane liquid routing," Lab Chip **15**, 2842–2853 (2015).
[8] K. Khoshmanesh, S.-Y. Tang, J. Y. Zhu, S. Schaefer, A. Mitchell, K. Kalantar-Zadeh, and M. D. Dickey, "Liquid metal enabled microfluidics," Lab Chip **17**, 974–993 (2017).
[9] P.-H. Huang, N. Nama, Z. Mao, P. Li, J. Rufo, Y. Chen, Y. Xie, C.-H. Wei, L. Wang, and T. J. Huang, "A reliable and programmable acoustofluidic pump powered by oscillating sharp-edge structures," Lab Chip **14**, 4319–4323 (2014).
[10] S. Wang, X. Huang, and C. Yang, "Valveless micropump with acoustically featured pumping chamber," Microfluid. Nanofluid. **8**, 549–555 (2010).
[11] K. Ryu, S. K. Chung, and S. K. Cho, "Micropumping by an acoustically excited oscillating bubble for automated implantable microfluidic devices," JALA **15**, 163–171 (2010).
[12] M. Nabavi, K. Siddiqui, and J. Dargahi, "Analysis of the flow structure inside the valveless standing wave pump," Phys. Fluids **20**, 126101 (2008).
[13] A. Ozcelik and Z. Aslan, "A practical microfluidic pump enabled by acoustofluidics and 3D printing," Microfluid. Nanofluid. **25**, 5 (2021).
[14] Y. Lin, Y. Gao, M. Wu, R. Zhou, D. Chung, G. Caraveo, and J. Xu, "Acoustofluidic stick-and-play micropump built on foil for single-cell trapping," Lab Chip **19**, 3045–3053 (2019).
[15] R. Jiang, S. Agrawal, M. Aghaamoo, R. Parajuli, A. Agrawal, and A. P. Lee, "Rapid isolation of circulating cancer associated fibroblasts by acoustic microstreaming for assessing metastatic propensity of breast cancer patients," Lab Chip **21**, 875–887 (2021).
[16] J. Lighthill, "Acoustic streaming," J. Sound Vib. **61**, 391–418 (1978).
[17] L. Rayleigh, "On the circulation of air observed in Kundt's tubes, and on some allied acoustical problems," Philos. Trans. R. Soc. London **175**, 1–21 (1884).
[18] H. Schlichting, "Berechnung ebener periodischer Grenzschichtstromungen," Phys. Z. **33**, 327–335 (1932).
[19] C. Eckart, "Vortices and streams caused by sound waves," Phys. Rev. **73**, 68 (1948).
[20] N. Zhang, A. Horesh, O. Manor, and J. Friend, "Powerful acoustogeometric streaming from dynamic geometric nonlinearity," Phys. Rev. Lett. **126**, 164502 (2021).

[21]D. Hughes and W. Nyborg, "Cell disruption by ultrasound," Science **138**, 108–114 (1962).
[22]C. Zhang, X. Guo, P. Brunet, M. Costalonga, and L. Royon, "Acoustic streaming near a sharp structure and its mixing performance characterization," Microfluid. Nanofluid. **23**, 104 (2019).
[23]C. Zhang, X. Guo, L. Royon, and P. Brunet, "Acoustic streaming generated by sharp edges: The coupled influences of liquid viscosity and acoustic frequency," Micromachines **11**, 607 (2020).
[24]C. Zhang, X. Guo, L. Royon, and P. Brunet, "Unveiling of the mechanisms of acoustic streaming induced by sharp edges," Phys. Rev. E **102**, 043110 (2020).
[25]P.-H. Huang, Y. Xie, D. Ahmed, J. Rufo, N. Nama, Y. Chen, C. Y. Chan, and T. J. Huang, "An acoustofluidic micromixer based on oscillating sidewall sharp-edges," Lab Chip **13**, 3847–3852 (2013).
[26]N. Nama, P.-H. Huang, T. J. Huang, and F. Costanzo, "Investigation of micromixing by acoustically oscillated sharp-edges," Biomicrofluidics **10**, 024124 (2016).
[27]H. Bachman, C. Chen, J. Rufo, S. Zhao, S. Yang, Z. Tian, N. Nama, P.-H. Huang, and T. J. Huang, "An acoustofluidic device for efficient mixing over a wide range of flow rates," Lab Chip **20**, 1238–1248 (2020).
[28]A. A. Doinikov, M. S. Gerlt, A. Pavlic, and J. Dual, "Acoustic streaming produced by sharp-edge structures in microfluidic devices," Microfluid. Nanofluid. **24**, 32 (2020).
[29]A. Pourabed, J. Brenker, T. Younas, L. He, and T. Alan, "A lotus shaped acoustofluidic mixer: High throughput homogenisation of liquids in 2 ms using hydrodynamically coupled resonators," Ultrason. Sonochem. **83**, 105936 (2022).
[30]P.-H. Huang, "Sharp-edge-based acoustofluidics," Ph.D. thesis (2016).
[31]I. Leibacher, P. Hahn, and J. Dual, "Acoustophoretic cell and particle trapping on microfluidic sharp edges," Microfluid. Nanofluid. **19**, 923–933 (2015).
[32]A. A. Doinikov, M. S. Gerlt, and J. Dual, "Acoustic radiation forces produced by sharp-edge structures in microfluidic systems," Phys. Rev. Lett. **124**, 154501 (2020).
[33]M. Ovchinnikov, J. Zhou, and S. Yalamanchili, "Acoustic streaming of a sharp edge," J. Acoust. Soc. Am. **136**, 22–29 (2014).
[34]Z. Chen, P. Liu, X. Zhao, L. Huang, Y. Xiao, Y. Zhang, J. Zhang, and N. Hao, "Sharp-edge acoustic microfluidics: Principles, structures, and applications," Appl. Mater. Today **25**, 101239 (2021).
[35]M. Evander and J. Nilsson, "Acoustofluidics 20: Applications in acoustic trapping," Lab Chip **12**, 4667–4676 (2012).
[36]S. Marefati, M. Ghassemi, and V. Ghazizadeh, "Investigation of effective parameters on streaming-induced acoustophoretic particle manipulation in a microchannel via three-dimensional numerical simulation," Phys. Fluids **34**, 012008 (2022).
[37]M. Wu, A. Ozcelik, J. Rufo, Z. Wang, R. Fang, and T. J. Huang, "Acoustofluidic separation of cells and particles," Microsyst. Nanoeng. **5**, 32 (2019).
[38]I. Leibacher, P. Reichert, and J. Dual, "Microfluidic droplet handling by bulk acoustic wave (BAW) acoustophoresis," Lab Chip **15**, 2896–2905 (2015).
[39]S. Xue, X. Zhang, F. He, Z. Liu, and P. Hao, "Acoustic particle migration and focusing in a tilted acoustic field," Phys. Fluids **33**, 122006 (2021).
[40]H. Bruus, J. Dual, J. Hawkes, M. Hill, T. Laurell, J. Nilsson, S. Radel, S. Sadhal, and M. Wiklund, "Forthcoming lab on a chip tutorial series on acoustofluidics: Acoustofluidics-exploiting ultrasonic standing wave forces and acoustic streaming in microfluidic systems for cell and particle manipulation," Lab Chip **11**, 3579–3580 (2011).
[41]M. B. Özer and B. Çetin, "An extended view for acoustofluidic particle manipulation: Scenarios for actuation modes and device resonance phenomenon for bulk-acoustic-wave devices," J. Acoust. Soc. Am. **149**, 2802–2812 (2021).
[42]R. P. Moiseyenko and H. Bruus, "Whole-system ultrasound resonances as the basis for acoustophoresis in all-polymer microfluidic devices," Phys. Rev. Appl. **11**, 014014 (2019).
[43]Z. Chen, Z. Pei, X. Zhao, J. Zhang, J. Wei, and N. Hao, "Acoustic microreactors for chemical engineering," Chem. Eng. J. **433**, 133258 (2021).
[44]K. Ren, J. Zhou, and H. Wu, "Materials for microfluidic chip fabrication," Acc. Chem. Res. **46**, 2396–2406 (2013).
[45]M. Wiklund, "Acoustofluidics 12: Biocompatibility and cell viability in microfluidic acoustic resonators," Lab Chip **12**, 2018–2028 (2012).
[46]M. Wiklund, S. Radel, and J. J. Hawkes, "Acoustofluidics 21: Ultrasound-enhanced immunoassays and particle sensors," Lab Chip **13**, 25–39 (2013).
[47]M. Gerlt, P. Ruppen, M. Leuthner, S. Panke, and J. Dual, "Acoustofluidic medium exchange for preparation of electrocompetent bacteria using channel wall trapping," Lab Chip **21**, 4487–4497 (2021).
[48]H. Bruus, "Acoustofluidics 2: Perturbation theory and ultrasound resonance modes," Lab Chip **12**, 20–28 (2012).
[49]A. Doinikov, "Acoustic radiation pressure on a rigid sphere in a viscous fluid," Proc. R. Soc. London, Ser. A **447**, 447–466 (1994).
[50]D. Andrews and M. McIntyre, "An exact theory of nonlinear waves on a Lagrangian-mean flow," J. Fluid Mech. **89**, 609–646 (1978).
[51]O. Bühler, *Waves and Mean Flows* (Cambridge University Press, 2014).
[52]L. P. Gor'kov, "On the forces acting on a small particle in an acoustical field in an ideal fluid," Sov. Phys.-Dokl. **6**, 773–775 (1962).
[53]T. Baasch and J. Dual, "Acoustic radiation force on a spherical fluid or solid elastic particle placed close to a fluid or solid elastic half-space," Phys. Rev. Appl. **14**, 024052 (2020).
[54]K. Yosioka and Y. Kawasima, "Acoustic radiation pressure on a compressible sphere," Acta Acust. Acust. **5**, 167–173 (1955).
[55]J. Schindelin, I. Arganda-Carreras, E. Frise, V. Kaynig, M. Longair, T. Pietzsch, S. Preibisch, C. Rueden, S. Saalfeld, B. Schmid *et al.*, "Fiji: An open-source platform for biological-image analysis," Nat. Methods **9**, 676–682 (2012).
[56]H. Bruus, *Theoretical Microfluidics* (Oxford University Press Oxford, 2008), Vol. 18.
[57]J.-Y. Tinevez, N. Perry, J. Schindelin, G. M. Hoopes, G. D. Reynolds, E. Laplantine, S. Y. Bednarek, S. L. Shorte, and K. W. Eliceiri, "Trackmate: An open and extensible platform for single-particle tracking," Methods **115**, 80–90 (2017).
[58]The Mathworks, Inc., *MATLAB Version R2019b* (The Mathworks, Inc., Natick, Massachusetts, 2019).
[59]COMSOL AB, *COMSOL Multiphysics Version 5.6* (COMSOL AB, Stockholm, Sweden, 2020).
[60]A. R. Selfridge, "Approximate material properties in isotropic materials," IEEE Trans. Sonics Ultrason. **32**, 381–394 (1985).
[61]P. B. Muller, R. Barnkob, M. J. H. Jensen, and H. Bruus, "A numerical study of microparticle acoustophoresis driven by acoustic radiation forces and streaming-induced drag forces," Lab Chip **12**, 4617–4627 (2012).
[62]J. Orosco and J. Friend, "Unraveling the complex dynamics of acoustofluidics," arXiv:2107.00172 (2021).
[63]A. Singh, N. Zhang, and J. Friend, "An investigation of maximum particle velocity as a universal invariant-defined by a statistical measure of failure or plastic energy loss for acoustofluidic applications," J. Acoust. Soc. Am. **150**, 878–890 (2021).
[64]A. Lenshof, M. Evander, T. Laurell, and J. Nilsson, "Building microfluidic acoustic resonators," in *Microscale Acoustofluidics* (Royal Society of Chemistry, 2014), pp. 100–126.
[65]H. Bruus, "Acoustofluidics 7: The acoustic radiation force on small particles," Lab Chip **12**, 1014–1021 (2012).
[66]P. Augustsson, R. Barnkob, S. T. Wereley, H. Bruus, and T. Laurell, "Automated and temperature-controlled micro-PIV measurements enabling long-term-stable microchannel acoustophoresis characterization," Lab Chip **11**, 4152–4164 (2011).
[67]Z. Wang, P.-H. Huang, C. Chen, H. Bachman, S. Zhao, S. Yang, and T. J. Huang, "Cell lysis via acoustically oscillating sharp edges," Lab Chip **19**, 4021–4032 (2019).
[68]S. Gutiérrez-Ramos, M. Hoyos, and J. Ruiz-Suárez, "Induced clustering of *Escherichia coli* by acoustic fields," Sci. Rep. **8**, 4668 (2018).
[69]S. C. Takatori, R. De Dier, J. Vermant, and J. F. Brady, "Acoustic trapping of active matter," Nat. Commun. **7**, 10694 (2016).
[70]C. L. Harshbarger, M. S. Gerlt, J. A. Ghadamian, D. C. Bernardoni, J. G. Snedeker, and J. Dual, "Optical feedback control loop for the precise and robust acoustic focusing of cells, micro-and nanoparticles," Lab Chip **22**, 2810–2819 (2022).